

# Determining the Spectral Energy Distributions and Absorption Coefficients for Sr-90 and Y-90

Louis Sayer

Level 3 Advanced Laboratory Report

Submitted: 20/04/21, Dates of Experiment: 11/01/21 - 19/03/21

The combined spectral energy distribution of Sr-90 and Y-90 is determined using a silicon surface barrier detector. The spectra show resemblance to those in the literature however the beta radiation from Y-90 appears diminished. Magnetic spectroscopy is used for the energy calibration process and the relationship between channel number and energy is quite linear. The  $\chi^2$  analysis of the calibration shows the errors have been over-estimated, caused by the assumption that the magnetic field was homogenous. The absorption coefficients for aluminium, carbon, silver and cadmium are determined but are in very poor agreement with the literature. The most likely cause for this is the difference in the geometry of the experiments and a lack of detail in their description in the literature.

## 1. Introduction

Strontium-90 is a radioactive isotope of strontium which decays through beta decay into yttrium-90, producing an electron and anti-neutrino in the process [1]. The production of the anti-neutrino allows the energy distribution of the electrons produced to be continuous. In this work we are interested in measuring this distribution and the absorption of beta particles by metal foils. Fig.1 shows the standard decay diagram for Sr-90.

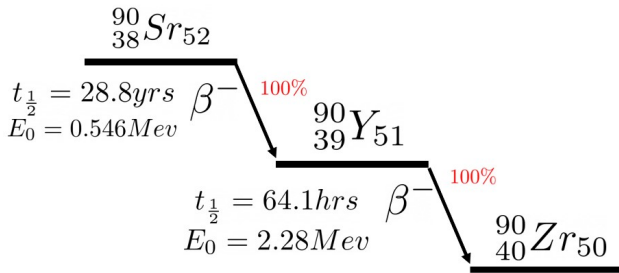


**FIG. 1:** A decay scheme of Sr-90 into the stable Zr-90. The half-lives of the decays  $t_{1/2}$  are shown as well as the endpoint energies  $E_0$  of Sr-90 and Zr-90 [1].

The constant decay of Sr-90 into Y-90 means the energy distribution of these isotopes are inextricably linked, making it difficult to study the isotopes individually. Despite this, the endpoint energies, spectrum shapes and the ratios of the number of beta particles are well documented in the literature [2], [3]. One way of separating the two elements is with the absorption of the beta particles by metal filaments. Upon absorption, the lower energy particles of the energy spectrum decrease quicker in number than the high energy particles and this phenomenon can be used to remove the Sr-90 parts of the spectrum [4], [5]. The absorption coefficients have been measured widely in the literature and have applications in dosimetry, beta shielding and contamination surveillance [6]. Sr-90 is a large by-product of nuclear fission reactions and was widespread after the Chernobyl incident, as well as others [7]. The absorption coefficient relates to the ratio of the number of counts without an absorber  $C_0$  to the counts with an absorber  $C$ :

$$C = C_0 e^{-nx} \quad (1)$$

where  $n$  is the absorption coefficient and  $x$  is the thickness of the absorber [8]. The thickness of the absorber is normally given in  $\text{mg}/\text{cm}^2$  so that it is related to its density  $\rho$

by  $x = \rho l$  where  $l$  is the thickness in cm. This gives the absorption coefficient units of  $\text{cm}^2/\text{mg}$ .

The absorption coefficient has been found empirically to be related to the endpoint energy of the beta emitter which is why there are distinct values for different emitters, in turn allowing for the identification of different isotopes [8]. This is another method for finding the endpoint energies of the emitters but that is not discussed in this paper. The absorption coefficients also depend on the geometry of the experimental set-up [9], [10], [6].

The loss in intensity of the beta particles can be attributed to scattering processes and absorption processes. This differentiates the attenuation coefficient which describes the absorption and scattering of the beam from the absorption coefficient which is due to absorption alone [9]. In the case of zero scattering the attenuation coefficient and absorption coefficient are the same. The effects of scattering on the loss of intensity depend on the geometry of the experiment because the solid angle spanned by the detector depends on its distance to the absorber and the absorber's distance to the source in cases where the beam is diffuse. It is shown in the literature that scattering is the major source of loss of electrons which reach the detector and therefore a good description of the geometry is important to compare absorption/attenuation coefficients. However, full descriptions of the experimental set-ups are lacking in the literature, which as we will see makes it difficult to compare values [9]. We will use the term absorption coefficient but as discussed later it seems plausible there were some particles lost to scattering considering our set-up.

The calibration process for finding the energy as a function of channel number involved calculating the energy of beta particles which would reach the detector for a given magnetic field and radius of curvature. The total energy  $E$  of a particle which equals its kinetic energy  $E_k$  and rest mass energy  $E_0$  can be written in terms of its rest mass  $m_0$  and momentum  $p$  as

$$(E_k + E_0)^2 = m_0^2 c^4 + p^2 c^2 \quad (2)$$

where  $c$  is the speed of light [11]. The radius of curvature  $r$  of a particle's path in a homogeneous magnetic field  $B$  is given by  $r = \frac{p}{|q|B}$  where  $|q|$  is the magnitude of its charge. Rearranging for  $p$  in Eq.2 gives a quadratic formula for the radius in terms of  $E_k$  as shown in Eq.3.

$$r = \frac{\sqrt{E_k(E_k + 2m_0 c^2)}}{|q|Bc} \quad (3)$$

## 2. Method

The chamber used in the calibration of the energies is shown in Fig.3. The lengths were measured with Vernier calipers. The energy calibration used in the experiment was done at 500x coarse gain and 1x fine gain. Two sets of readings were taken. The first was in increments of 1 A from 1 to 15 A, with the real time set at 1.5 hrs while the second

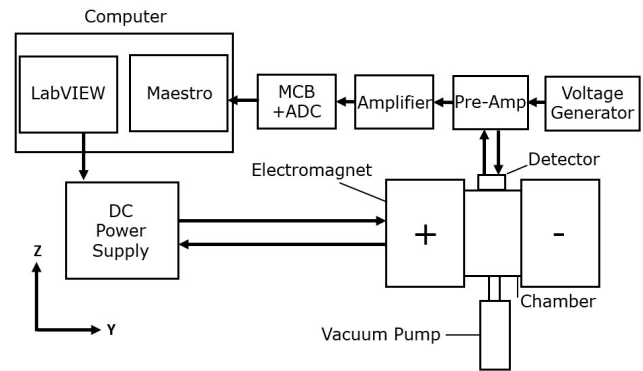
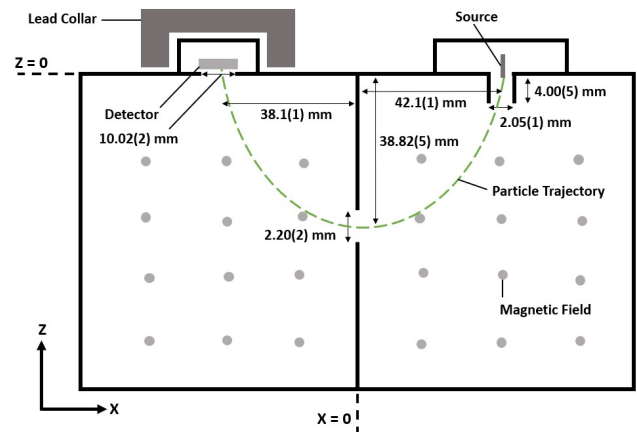


**FIG. 2:** The experimental set-up used for the energy calibration process. An arrow represents an electrical connection between two appliances.



To measure the absorption of the beta particles by a source we firstly measured the spectrum without a source but with the foil to ascertain the background counts and noise profile. This spectrum was subtracted from any further mea-

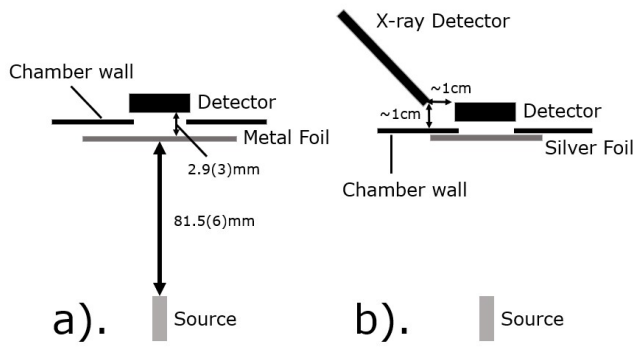


**FIG. 4:** The experimental set-up for measuring the attenuation of beta particles by metal foils (a) and the x-ray spectra of silver as the beta particles interact with this metal (b).

measurements to remove the background. Measurements with the foil were taken for a real time of three hours to reach high numbers of counts. This reduced the Poisson error and the spectra were more continuous channel to channel. Four metals were used at 0.5 mm of thickness (aluminium, carbon, cadmium and silver) and three metals were used at 0.1 mm of thickness (gadolinium, iron and aluminium). To provide a further comparison Aluminium was also measured at 0.2 mm of thickness.

The gamma spectrum of Am-241, of which the peaks were used to calibrate the silver x-ray spectrum, was measured for 29 minutes with a X-123 x-ray spectrometer. The silver foil was then placed in front of the usual detector and the Sr-90 source was placed at a set distance away as shown in Fig.4 b). The x-ray detector measured the radiation off the silver foil for a real time of 2.7 days corresponding to a live time of three hours.

### 3. Results and Discussion

#### 3.1. Energy Distribution

The energy distribution for Sr-90 and Y-90 measured with our apparatus is shown in Fig. 5. The counts were sorted by a multi-channel buffer which analysed the voltage pulses from the amplifiers and detector. The energy values were calibrated with a magnetic spectrometer as described in the method. A distribution without the source has been subtracted to remove the background noise from the spectrum, however some of this has remained and can be seen at 0keV as the isolated spike. The background spectrum was multiplied by the ratio of the live times of the source measurement to the background measurement to factor in the time for which counts were actually processed by the MCB.

The peak of the Sr-90 distribution can be seen clearly at around 140keV but the peak of Y-90 is much less pronounced, especially compared to the literature [2] [4]. A slight dip can be seen at around 200 keV which would normally be attributed to the endpoint energy of Sr-90 however this energy is too low for this to be the cause. Although the highest energy capable of being measured at this gain was 898 keV it is clear there is a significant drop in counts at these higher energies which is uncharacteristic for this spectrum as the endpoint energy of Y-90 is 2.28 MeV. For these reasons it appears the Y-90 spectrum was measured less than expected. Even in the calibration of the energy scale where the magnetic field was used to select energies it was difficult to discern any peaks beyond 700 keV as the

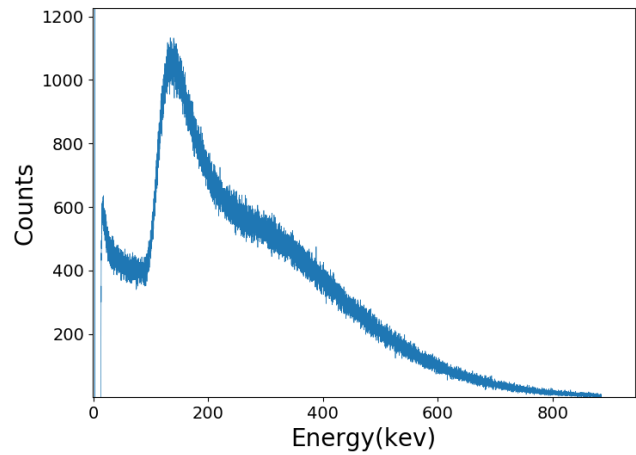


**FIG. 5:** The number of counts as a function of energy for Sr-90 and Y-90. The data are plotted as a line because the number of energy channels is large enough that it can be considered continuous. The energy values have error bars but these are not shown to make the figure clearer to the reader.

numbers of counts were so low. It was not established why the Y-90 counts were lower than expected.

There were several corrections which had to be considered when taking measurements of the distribution. The half-life of Sr-90 is 28.6 years whereas a measurement could have run for up to three hours. This difference is negligible compared to other sources of uncertainty in the experiment, even compared to different runs over the ten weeks in which the experiment took place which would have given a fractional uncertainty of 0.68%. The error in the energy calibration for example was much higher than this.

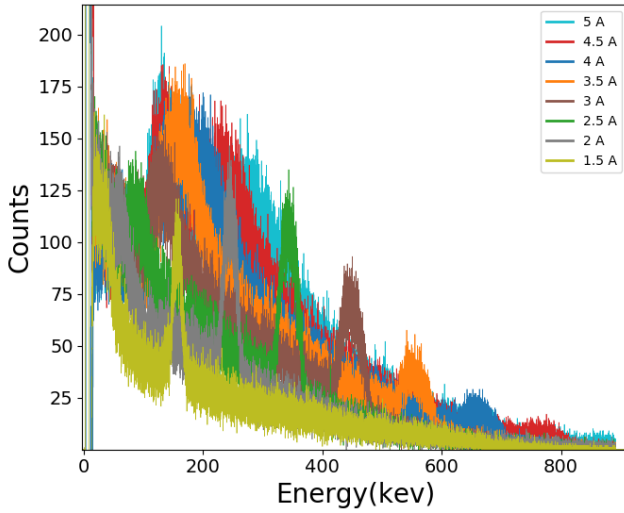
The background counts were determined by measuring the number of counts for the same period of time but without the source present. These counts were very high at lower numbers but were less significant at higher channels. Most of the counts at lower channel numbers likely came from electrical noise. The counts at low channel numbers at the start of an experiment increased very quickly, more than could be expected from background radiation. Changes in the positions of the power cables could also increase the noise which supports the idea that it came predominantly from the electrics. All spectra used in calculations had this spectrum subtracted. The vacuum prevented attenuation by air particles in the chamber and if allowed to equilibrate had a reasonably low average value of  $0.058 \pm 0.006$  hPa. That was taken on nine different occasions during the period of when most measurements were taken. An overnight set of nine measurements of the vacuum chamber had an average number of counts of  $(135 \pm 1) \times 10^6$ . At low channel numbers ( $<500$ ) where the subtraction process is more important because the counts are higher, the average number of counts was fairly constant at  $(134 \pm 1) \times 10^6$ . Subtracting the spectra from each other produced minor differences between them which confirmed the vacuum was quite stable. We only took one long measurement of the vacuum to subtract from source measurements as the differences between measurements were small compared to other sources of uncertainty.

Another method to decrease the noise measured was by using a self-coincidence system in which a 'gate' was opened when a signal coming from the amplifier was higher than a discrimination level (set by hand) just above that of the noise. It was found that using this decreased the dead-

percentage but that the majority of the spectrum was unchanged. We chose not to use this system because we wanted to be able to monitor the whole spectrum including any changes in the noise and that this would not be a problem if we could subtract the background manually. With hindsight it may have been better to use this system as lower channel numbers containing the noise were discarded from most calculations regardless.

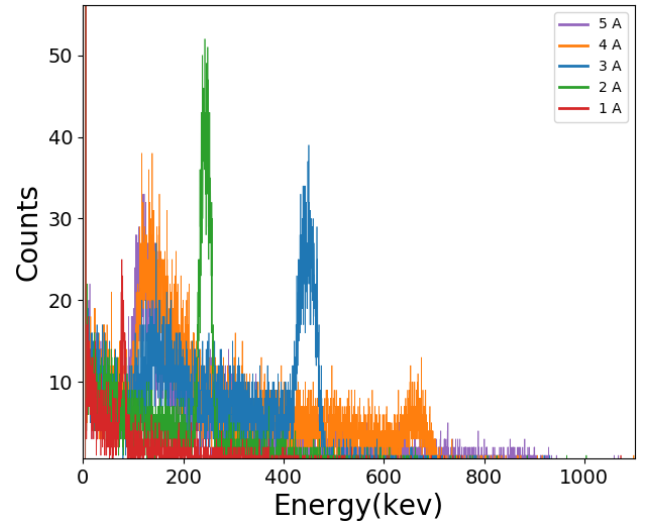
### 3.2. Energy Calibration

The energies of the spectra were calibrated by using the magnetic spectrometer. Energy ranges were selected by supplying the electromagnet with the required currents to bend the particles' trajectories in the resulting magnetic field onto the detector in the chamber. The energy spectra at 500x and 100x coarse gain are shown in Figs. 6 and 7 respectively. A measurement of the background noise in the chamber was subtracted from each spectrum, taking into account the ratio of the live times between measurements.



**FIG. 6:** The number of counts as a function of energy for Sr-90 and Y-90 at 500x coarse gain for eight different currents. The energy values have error bars but these are neglected to make the figure clearer to the reader.

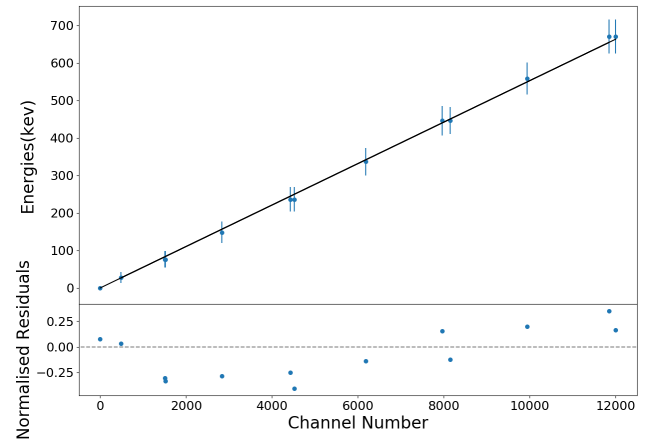
In both Figs. 6 and 7 the peaks corresponding to the selected energies of beta particles can be seen clearly as the steep spikes. For example in Fig.6 the first peak can be seen in the spectrum in olive green at roughly 150 keV. The peaks become less pronounced at higher magnetic field values as the number of counts decreases. Strangely the normal peak of the Sr-90/Y-90 energy distribution shifts as well, most notably in Fig.6. It was not obvious why this was the case. It may have been caused by alternative paths of the beta particles through the chamber but the addition of a lead collar around the detector should have prevented undesired particles from reaching it. The highest energy peaks which could be accurately determined were at 4 A corresponding to energies of 670 keV in the case of 500x coarse gain. The counts beyond this energy were lower than expected and it was difficult to identify peaks as can be seen at 5 A in Fig.7. This was the reason for choosing a higher gain as only lower energies could be properly analysed. Having a lower gain also led to less continuous spectra as the counts were distributed over fewer channels. This made it harder to identify the channel numbers of peaks which was done with Mariscotti-type peak searches in Maestro [12]. Absorption by metals



**FIG. 7:** The number of counts as a function of energy for Sr-90 and Y-90 at 100x coarse gain for five different currents. The energy values have error bars but these are neglected to make the figure clearer to the reader.

of beta particles is higher at lower energies which gave more reason to investigate lower energies [4].

The identification of the peaks was a crucial part of the calibration process. Fig. 8 shows the relationship between channel number and energy which was used to scale the energy axes of the previous plots and allows us to analyse the data with respect to energy. The channel numbers were identified using Maestro software and the magnetic field values at certain currents were put in the solutions to Eq.3 as well as the radius of the trajectories to give the corresponding energies of the beta particles.



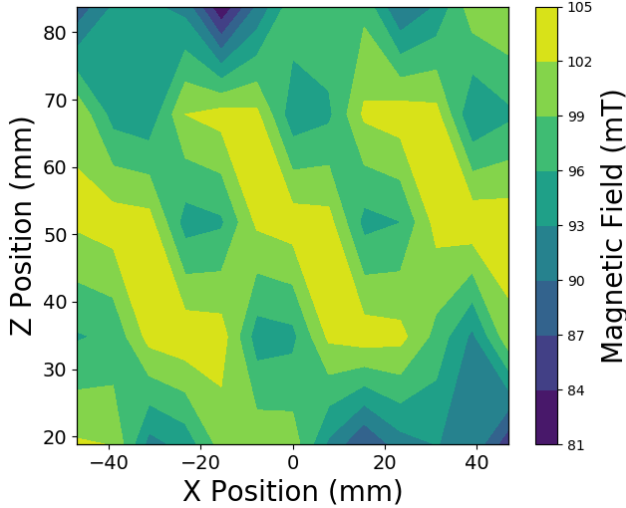
**FIG. 8:** The energy of the beta particles as a function of channel number. A linear trend line has been added as well as error bars for both variables although the channel number error bars are too small to be seen. The normalised residuals to the trend line are graphed below.

Fig.8 appears to show that the relationship between energy and channel number is linear. All points are well within one standard error of the trend line as can be seen by the normalised residuals. There may be a slight trend in the residuals from channel number 2000 onwards as the residuals increase quite consistently, however they are all very low. The trend line parameters were determined using a  $\chi^2$  fitting as the errors were heteroscedastic and this allowed points with lower error to be given more credence. A  $\chi^2_{min}$  value of 0.77 was obtained with this linear fitting,  $2.2\sigma$  lower than



the number of degrees of freedom 11. This gave a  $\chi^2_\nu$  of 0.070 which made us question whether the model was a good fit. The probability of obtaining this value, or higher,  $P(\chi^2_{min}; \nu)$  was found to be less than one by just  $1 \times 10^{-5}$  which told us that the standard errors in the energies were vastly overestimated [13]. For this reason we did not reject the null hypothesis and we kept the linear fit.

The dominant source of error in the energy calculations came from the magnetic field uncertainties. Fig. 9 shows the variation in the magnetic field in space in parts of the chamber at around 100mT.



**FIG. 9:** The magnetic field values in mT in the space of the chamber in the Y direction with the same axes as Fig.3. The X axis has 13 intervals while the Z axis has 5 and values in between have been interpolated. The values are approximately that of the plane in which the beta particles would travel (Y=19mm). The error values are not included for all points.

The field values were calculated from an average of the two planes between which the beta particles travelled (around 19mm). Not all Z values are included. Below 15.1mm the variation was even greater but this was measured less. In the proximity of the estimated trajectory (determined by looking at the circular path of the beta particles) the average field value at Z=15.1mm and above was  $94 \pm 2$  mT while below 15.1mm the average field value was  $51 \pm 1$  mT. This large variation in the magnetic field is what motivated us to try to calculate the trajectories of the beta particles at the relevant radii and magnetic fields at different points in space. We tried to divide the chamber into four sections each with different radii and magnetic fields but this proved difficult and gave nonsensical values. There was also the option of interpolating the values and integrating over the magnetic field values to give their trajectories but this was a laborious process and would have been better suited if more of the space had been measured. Instead we chose to assume the field was homogeneous assuming an average value of  $88 \pm 3$  mT, including the fringe values, at around 100 mT. This gave large errors for the energies from the magnetic field, the lowest energies had the highest errors with fractional uncertainty reaching 54%. The average uncertainty was also very high at 15.8%. This shows how assuming the magnetic field to be homogeneous was a bad approximation and led to an overestimation of errors. It would have been better to take more magnetic field values, particularly around the expected trajectories of the electrons, and calculate their path. This would have also decreased the radius error as it would

no longer have had to be constant.

The energy errors coming from the radius uncertainties were also significant. As can be seen in Fig.3 the radii at different parts of the chamber were quite different and the finite width of the slits gave a substantial error. The smaller slits at the entrance and centre were assumed to constrain the path as the detector width was much larger. A standard error from these two uncertainties when propagated through Eq.3 gave fractional uncertainty in the energy of up to 19%. All the fractional uncertainties from the radius apart from at zero magnetic field were 10% or higher. The error propagation is described in more detail in the error appendix. If the trajectories of the beta particles could be estimated more accurately then the energies would be better selected and the errors would be smaller.

### 3.3. Metal Filaments

As Eq.1 shows, comparing the total number of counts in an unscreened case to that with a metal foil in front of the detector can give the absorption coefficients of the metal for a specific radioactive isotope. The densities of the metals were found in the Smithsonian Physical Tables [16] and for carbon the manufacturer [17]. Table I shows the results for the absorption coefficients for Y-90 with four different metals. The ratio of the live times of the screened and unscreened cases were again factored in.

**TABLE I:** The absorption coefficients of different metals for Y-90 (endpoint energy 2.28 MeV). The absorption coefficient should be independent of absorber thickness.

Metal (Thickness)	Absorption Coefficient ( $\text{cm}^2/\text{g}$ )	
	Calculated Value	Literature
Silver (0.5mm)	$10.25 \pm 0.04$	7.1 [8]
Cadmium (0.5mm)	$10.46 \pm 0.03$	N/A
Carbon (0.5mm)	$5.5 \pm 0.3$	3.9 [9]
Aluminium (0.5mm)	$6.98 \pm 0.01$	$4.54 \pm 0.09$ [3]
Aluminium (0.2mm)	$1.8 \pm 0.4$	$4.54 \pm 0.09$ [3]

Our results for the absorption coefficients are in very poor agreement with all the literature values as they are all many standard errors apart. The main reason for these discrepancies is probably due to differences in experiment geometry. Ameen et al. show that scattering is the dominant cause of reduction in beta particles in interactions with metal filaments by comparing the number of counts for absorption and scattering with absorption alone cases. If the absorber is placed close to the detector, the detector can still measure scattered particles however with a greater distance scattered particles will miss the detector. For Ameen et al. the number of counts for absorption alone is tens of times greater than with absorption and scattering [9]. This is supported by Yalcin et al. who show that increasing the absorber-source distance from 0.5 cm to 4.9 cm decreases the mass attenuation coefficient by  $3.2 \text{ cm}^2/\text{g}$  [6]. However they also found that increasing the absorber-detector distance decreases the attenuation coefficient (by  $3.3 \text{ cm}^2/\text{g}$  from 0.8 cm to 5 cm) whereas we would assume that scattering at a further distance would increase the attenuation coefficient. Despite this, it is clear that the geometry of the experiment has a strong effect on the attenuation coefficient.

Direct comparisons to the literature are challenging in the absence of accurate measurements for the set-up of the ex-

periments. Our measured value for the absorber-detector distance was  $2.9 \pm 3$  mm while the absorber-source distance was  $81.5 \pm 6$  mm.

Another difficulty in measuring the absorption coefficients for Sr-90 and Y-90 was isolating the counts from the elements since the absorption coefficients depend on the endpoint energy. This was why thicker metal foils were used to measure the coefficients. Carmona and Rizo found a linear relationship between metal thickness and absorption coefficient for thicknesses between  $100 \text{ mg/cm}^2$  and  $550 \text{ mg/cm}^2$  [5]. At these thicknesses the Sr-90 beta particles were not 'energetic enough to arrive to the detector' and therefore only Y-90 electrons were counted. Fig. 10 shows the variation between the absorber thickness and the log of the counts with foil over counts without foil.

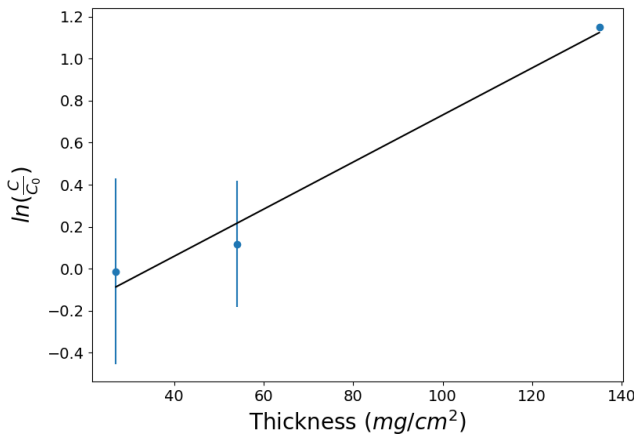


**FIG. 10:** The natural logarithm of counts with a metal foil over counts without a metal foil versus the thickness of aluminium foil. The error bars are shown for the y axis while a linear trendline is given to guide the eye.

For thicknesses below  $100 \text{ mg/cm}^2$  counts were only included for 546 keV and higher, the endpoint energy of Sr-90 [3]. This gave rise to a high error coming from the energy calibration, in this case the dominant error. This is why the values were not combined because the error at thickness  $135 \text{ mg/cm}^2$  was considerably lower. The absorption coefficient at  $27 \text{ mg/cm}^2$  also had a negative value which gave non-physical results. The dominant error in general came from the Poisson error in the shielded counts. This gave on average an error of 0.43%. For carbon the dominant error came from the thickness as the density of graphite had a high uncertainty and for aluminium 0.2 mm the dominant error came from only including counts at energies higher than 546 keV, which is discussed further in the error appendix. For this reason it appears much more advantageous to measure the absorption coefficients at larger thicknesses. The errors from the unshielded counts were slightly lower as the Poisson errors showed an average error of 0.35%.

### 3.4. X-ray Measurements

To calibrate the energy scale of the x-ray detector an Am-241 source was used, the gamma ray peaks of which had energies widely measured in the literature [14], [15]. Fig. 11 shows this spectrum.

With this calibration the energy spectrum of x-rays off a silver target was plotted as seen in Fig. 12.

The bremsstrahlung radiation spectrum can be seen as the continuous decrease in counts over energy but in this case

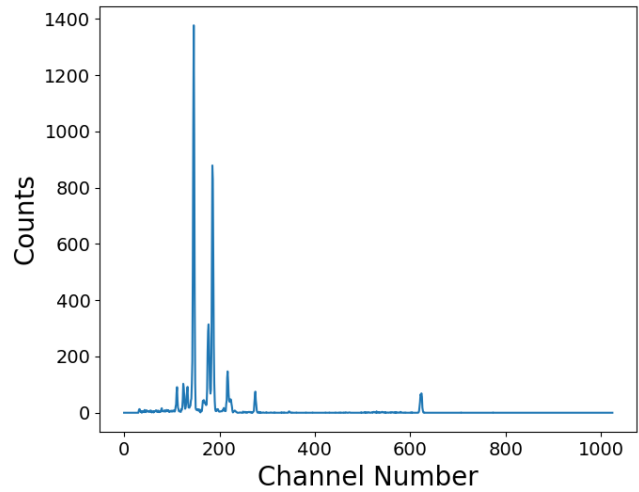


**FIG. 11:** The number of counts for different channel numbers of an Am-241 source. The characteristic gamma ray peaks matched with the literature can be seen at channel numbers 146.125, 185.5, 217.25, 275.2 and 623.5.

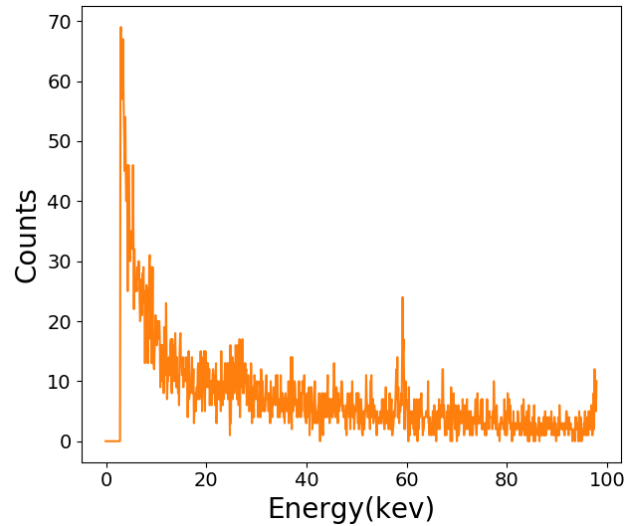


**FIG. 12:** The number of counts as a function of energy for x-rays off a silver foil. The energy values have error bars but these are neglected to make the figure clearer to the reader.

the counts distribution is quite discontinuous. This was because there were few x-rays measured and the dead-time was quite high. It is difficult to discern any characteristic x-ray peaks apart from possibly one at around 60 keV but these are reported less in the literature. Also in the literature the K-series, of which the energies are around 20 keV, is the most prominent but these are difficult to see in Fig. 12 [15]. It is interesting to see that the x-ray spectrum can be measured with such an apparatus but the run time would have to be longer to better see the characteristic peaks and analyse the spectrum. This would be challenging considering the run time for the experiment was already long at 2.7 days.

### 4. Conclusions

In conclusion, the beta radiation of Sr-90 and Y-90 have been measured in numerous ways but have produced some poor results. The combined unshielded spectra had a similar shape to those shown in the literature but the Y-90 spectrum was unusually less prominent as shown by the low counts at high energies, low second peak in the combined spec-

trum and indistinguishable peaks in the energy calibration. The energy calibration showed a reasonable linear fit but the overestimation of errors from the radius and magnetic field gave rise to the poor  $\chi^2$  value. More detailed measurements of the magnetic field values would have allowed for a better determination of the particle trajectories and lowered the error. The absorption coefficients were measured to high precision however they were all in poor agreement with the literature [3], [9], [8]. This was most likely caused by different geometries in the set-up which as shown in the literature can greatly alter the values [9], [10], [6]. It is important that experimental geometries are detailed in reports so that proper comparisons can be made. The set-up was also modified to measure the x-rays of a silver foil blocking the source. A poor distribution was measured which shows that although this method does work for finding x-ray distributions, a set-up specifically designed for this purpose would work much better.

### Acknowledgments

The author would like to thank in particular Dr Ian Terry for tirelessly taking the measurements for this experiment in person while the author was unable to access the laboratory during the Covid-19 pandemic. Without his help this project would not have been possible.

### References

- [1] Ground and isomeric state information for Sr-90, 2020, National Nuclear Data Center, <https://www.nndc.bnl.gov/nudat2/reCenter.jsp?z=%2038&n=%2052>, accessed 15/04/2021 .
- [2] H. H. Hansen, Measurement of the beta-ray spectra of 90 Sr - 90Y, The International Journal of Applied Radiation and Isotopes, 1983, Volume 34, Issue 8.
- [3] T. Baltakamens, Accuracy of Absorption Methods in the Identification of Beta Emitters, Nuclear Instruments and Methods, 20/12/1976, Volume 142, Issue 3, Pages 535-538.
- [4] Y. Kawada et al., Observation of Beta-Ray Spectra after Penetrating Absorbing Materials, Applied Radiation and Isotopes, 2008, Volume 66, Issues 6-7, Pages 819-882.
- [5] J. H. Carmona and O. D. Rizo, Experimental and Monte Carlo Determination of Mass Absorption Coefficients for 90Sr/90Y Beta Particles in Organic Compounds, Nucleus, 14/05/2009, No.45 .
- [6] S. Yalcin and O. Gurler, Effect of Different Arrangements of Point Source, Aluminum Absorber and Detector on Mass Absorption Coefficient of Beta-Particles, Journal of Radio-analytical and Nuclear Chemistry, 19/05/2005, Volume 266, No. 3, pages 509-511.
- [7] Agency for Toxic Substances and Disease Registry , Toxicological Profile for stron, U.S. Department of Health and Human Services, 2004, <https://www.atsdr.cdc.gov/toxprofiles/tp159.pdf>, accessed 15/04/2021.
- [8] T. Baltakamens, A Simple Method for Determining the Maximum Energy of Beta Emitters by Absorption Measurements, Nuclear Instruments and Methods, 30/05/1970, Volume 82, Pages 264-268.
- [9] S. Ameen, A. Ahmed and R. Abdulllah, Influence Of The Experiment-Geometry On The Attenuation of Beta-Particles, Journal of Zankoi Slulaimani, 2014, Volume 16(4).
- [10] S. R. Thontadarya, Effect of Geometry on Mass Attenuation Coefficient on Beta-Particles, The International Journal of Applied Radiation and Isotopes, 1984, Volume 35, Issue 10, Pages 981-982.

- [11] H. Young and R. Freedman, University Physics with Modern Physics (13th edition), Pearson Education, San Francisco, 2012.
- [12] M. A. Mariscotti, A Method for Automatic Identification of Peaks in the Presence of Background and its Application to Spectrum Analysis, Nuclear Instruments and Methods, 1967, Volume 50, Pages 309-320.
- [13] I. G. Hughes and T. P. A Hase, Measurements and their uncertainties, Oxford, University Press, Oxford, 2010.
- [14] D. Demir, M. Eroglu and A. Tursucu, Studying of Characteristics of the HPGe Cetector for Radioactivity Measurements, Journal of Instrumentation, 2013, <http://iopscience.iop.org/1748-0221/8/10/P10027>, accessed 15/04/2021.
- [15] K. Terada et al. Measurements of Gamma-Ray Emission Probabilities of 241, 243 Am and 239 Np, Journal of Nuclear Science and Technology, 2016, Volume 53, Issue 11, Pages 1881-1888.
- [16] Smithsonian Institution, Smithsonian Physical Tables, City of Washington, 1954
- [17] Carbon (C) Foil Material Information, 2021, GoodFellow, <http://www.goodfellow.com/E/Carbon-Foil.html>, Accessed 19/04/2021

### 5. Appendix

The sources of error in an energy value for the calibration were the magnetic field and radius of beta particle trajectory.

The error in the magnetic field was found by calculating the standard error of the magnetic field values in the two planes closest to the plane of beta particles and the points in space closest to the particle trajectories. This was because the magnetic field was assumed to be homogeneous. The radius error was calculated as the standard error between the two radii which were deemed to constrain the particles' trajectories - namely the source slit to centre slit separation and centre slit depth. These two sources of error were propagated through to an energy error using the functional approach. Taking  $f(r, B)$  as the function which solved the quadratic equation for the kinetic energy the error from radius  $\alpha_E^r$  was

$$\alpha_E^r = |f(r + \alpha_r, B) - f(r, B)| \quad (4)$$

where  $\alpha_r$  was the standard error of the radii values. The same method was used to find the energy error from the magnetic field. The radius and magnetic errors were combined in quadrature such that the total energy error  $\alpha_E$  was

$$\alpha_E = \sqrt{(\alpha_E^r)^2 + (\alpha_E^B)^2} \quad (5)$$

To determine the error in energy at a particular channel number a linear fitting was used to find the energy as a function of the channel number with  $\chi^2$  analysis. This was used as the errors were heteroscedastic and therefore points with lower error were given more credence. The error in the channel number of a peak was determined to be much lower than the energy error and was neglected in any calculations. The  $\chi^2$  analysis was done by first minimising the  $\chi^2$  statistic giving the best-fit parameters (intercept and gradient) [13]. The error of each parameter was then calculated by finding the extremal difference between the best-fit values and their values at the  $\Delta\chi^2 + 1$  contour. Practically, this

can be done by increasing one parameter whilst keeping the other constant until it reaches the  $\Delta\chi^2 + 1$  contour. Then, the  $\chi^2$  is re-minimised and this is repeated until there is no discernible difference in the  $\chi^2 + 1$  calculated. This looks like a series of orthogonal steps between the best-fit parameters to the  $\Delta\chi^2 + 1$  contour, touching said contour between the re-minimisation steps. Fig.13 shows the  $\chi^2$  contours.

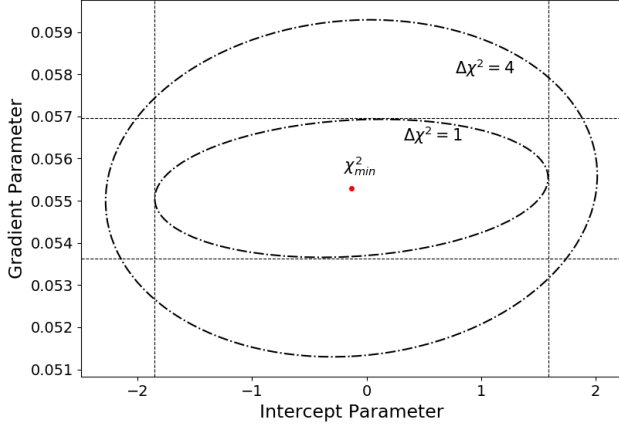


**FIG. 13:** A  $\chi^2$  contour plot for the gradient and intercept parameters. The best-fit parameters are shown as the red dot in the centre. The  $\Delta\chi^2$  contours for one and two standard deviations are included to show the sensitivity of each parameter.

The  $\chi^2$  analysis was only performed for the data at 500x gain as these were used in further calculations. At 100x gain the energy calibration and its errors were found with a least squares fit as this distribution was only used in comparison to that at 500x gain.

The errors in the absorption coefficients came from the errors in original counts, shielded counts and the error in the thickness of metal film. In the case of aluminium foil 0.2

mm in thickness there was also an error associated with ensuring only Y-90 was counted ( i.e only taking counts for  $E > 546$  kev). The errors in the original counts and counts with film in front were the square roots of the total counts because they are described by Poisson count statistics. The square root was calculated and then scaled by the ratio of the live times so that the errors in the counts were not unfairly changed by the scaling. The error in the absorber thickness in  $\text{mg}/\text{cm}^2$  came from the absolute error in the thickness in mm of the metal foils or in the case of carbon, a high uncertainty in its density . The error in the density of carbon was taken as one in the last digit. These absolute errors were propagated through with the functional approach. The error in ensuring only Y-90 was considered for aluminium 0.2 mm was calculated by propagating the error in the gradient (of the energy calibration) in choosing which channel number to count from. All these individual errors were propagated through to an error in the absorption coefficient with the functional approach. To give a final error in the absorption coefficient these were combined in quadrature such that the error in the absorption coefficients  $\alpha_\mu$  was

$$\alpha_\mu = \sqrt{(\alpha_\mu^C)^2 + (\alpha_\mu^{C_0})^2 + (\alpha_\mu^x)^2 + (\alpha_\mu^E)^2} \quad (6)$$

where  $\alpha_\mu^{C_0}$  was the error in the original counts,  $\alpha_\mu^C$  was the error in shielded counts and  $\alpha_\mu^x$  was the error in the thickness of the metal foil. The error in energy selection  $\alpha_\mu^E$  was only included for aluminium foil 0.2 mm.

The error in the energy of Am-241 peaks was taken as 0.1 kev from comparing the differences of sources in the literature. Again, the uncertainty on the channel number of the peak was negligible. As the errors were homoscedastic a least squares fitting was used to find the error in the gradient and intercept of the energy channel relation. However these errors were never used further in any calculations.